Physics of Fluids

RESEARCH ARTICLE | AUGUST 07 2023

Study on the evolution and stability of gas–liquid interfaces based on composite structures on the sidewall surface of a microchannel

Ming Zhu (朱明) ; Jian Huang (黄荐) ; Qiang Zhou (周强) ; Zhaohui Yao (姚朝晖)

Physics of Fluids 35, 082005 (2023)
https://doi.org/10.1063/5.0163959

Physics of Fluids ARTICLE pubs.aip.org/aip/pof

Study on the evolution and stability of gas–liquid interfaces based on composite structures on the sidewall surface of a microchannel

Cite as: Phys. Fluids **35**, 082005 (2023); doi: 10.1063/5.0163959
Submitted: 20 June 2023 · Accepted: 22 July 2023 ·
Published Online: 7 August 2023

View Online Export Citation CrossMark

Ming Zhu (朱明),[1] Jian Huang (黄荐),[2,a)] Qiang Zhou (周强),[3] and Zhaohui Yao (姚朝晖)[1,a)]

AFFILIATIONS

[1]School of Engineering Science, University of Chinese Academy of Sciences, Beijing 101408, People's Republic of China
[2]Key Laboratory for Mechanics in Fluid Solid Coupling Systems, Institute of Mechanics, Chinese Academy of Sciences, Beijing 100190, People's Republic of China
[3]School of Chemical Engineering and Technology, Xi'an Jiaotong University, Xi'an, People's Republic of China

[a)]**Authors to whom correspondence should be addressed:** huangjian@imech.ac.cn and yaozh@ucas.edu.cn

ABSTRACT

The gas–liquid interface plays a crucial role in reducing the flow resistance of superhydrophobic surfaces. However, this interface is highly unstable and prone to collapse under flow shear, environmental pressure fluctuations, phase transitions, and diffusion between dissolved gases and free gases. Once the gas–liquid interface collapses, the flow resistance increases rapidly. Therefore, it is necessary to study the stability of the gas–liquid interface. This paper considers a three-dimensional-printed composite structure combining transverse posts and reentrant structures in a microchannel. This structure effectively improves the stability of the gas–liquid interface, allowing it to maintain stability even on surfaces made of hydrophilic materials. Under the effect of the transverse posts, the length of the gas–liquid interface above the groove increases from micrometers to millimeters. The lattice Boltzmann method is applied to analyze how the composite structure effectively improves the stability of the gas–liquid interface. Through analysis of the interface collapse process, the factors affecting the stability of the gas–liquid interface in this structure are explored, providing a theoretical foundation for structural optimization.

I. INTRODUCTION

Previous studies[1,2] have found that when water contacts a superhydrophobic surface, it only touches the top of the rough microstructures, sealing air between the microstructures and forming a gas–liquid interface within the structures. The existence of this gas–liquid interface gives superhydrophobic surfaces excellent self-cleaning and drag reduction properties. Researchers have used various structures[3] to form gas–liquid interfaces, such as microridges,[4] microgrooves,[5] microposts,[6] and micropores.[7] However, the stability of the gas–liquid interface formed by these structures is poor and can be easily affected by factors, such as shear stress,[8] environmental pressure fluctuations,[9–11] dissolved gas saturation,[12,13] liquid–vapor conversion,[14] and diffusion between dissolved gases and free gases.[14] The collapse of the gas–liquid interface significantly increases the flow resistance. Therefore, it is important to explore the stability of gas–liquid interfaces and understand the associated destabilization mechanism.

Forsberg *et al.*[15] studied the effect of hydrostatic pressure on the stability of the gas–liquid interface for the case of superhydrophobic surfaces. Experiments showed that maintaining the stability of the gas–liquid interface requires a certain range of hydrostatic pressure, and the system has a critical pressure. When the environmental pressure exceeds this critical value, the gas–liquid interface is damaged, resulting in a sharp decrease in the drag reduction ability of superhydrophobic surfaces. The stability of the gas–liquid interface is not only affected by the hydrostatic pressure, but also by the diffusion between dissolved and free gases. Xiang *et al.*[16] theoretically demonstrated the existence of a final stable state for underwater superhydrophobic surfaces through thermodynamic analysis and experimentally demonstrated that adjusting the dissolved gas saturation within a critical range affected the equilibrium morphology of the meniscus, thereby extending the stable range of the interface. Hyvaluoma and Harting[8] used the two-phase lattice Boltzmann method (LBM) to simulate the interface deformation of microstructure surface bubbles under flow shear. The simulation results indicated that the slip length decreased as the shear rate increased, a phenomenon related to the interface deformation caused by flow shear.

To enhance the stability of the gas–liquid interface, in addition to studying the effects of external environments, such as pressure, gas saturation, and flow shear on interface stability, many researchers have attempted to innovate and improve the microstructure morphology based on the microstructure itself, thus improving the stability of the gas–liquid interface. The two-level hierarchical structure designed by Xue *et al.*[17] provides more pinning points for the three-phase contact line and increases the energy barrier between the Cassie state and the Wenzel state, which enhances the interface stability. However, these traditional structures typically require further hydrophobic coating to make them superhydrophobic. In practical applications, this hydrophobic coating treatment will increase the difficulty of processing, and the coating is easily damaged by contamination, which will affect the surface performance. Tuteja *et al.*[18] found that a singly reentrant structure can greatly enhance the stability of the gas–liquid interface. For liquids with low surface energy, such as ethanol, the Cassie state can be maintained on surfaces with reentrant structures. Liu and Kim[19] further found that a doubly reentrant structure can repulse very-low-energy liquids, even on surfaces made of completely wettable materials (e.g., silica). With the development of three-dimensional (3D) printing technology, many scholars have improved these structures and made superhydrophobic surfaces with better performance,[20] such as triply reentrant structures,[21] hierarchical triply reentrant structures,[21] doubly reentrant structures supported by a spring-like flexible base,[22] and doubly reentrant structures with a short wall passing below the side caps.[23]

Inspired by Liu and Kim's[19] research, Zhang *et al.*[24] introduced a doubly reentrant structure from the surface to the inside of the microchannel. They studied the influence of the microstructure geometry on the gas–liquid interface evolution under the flow state, thus extending the literature on the stability of the gas–liquid interface from quiescent conditions to flowing states. Recently, Panter *et al.*[25] further examined the effects of geometric parameters, such as the solid area fraction, cap height, and pillar height, on surface characteristics including the contact angle hysteresis, critical pressure, and minimum energy wetting barrier of doubly reentrant structures. Their development of an optimal design greatly improved the superhydrophobic surface performance.

To improve the performance of superhydrophobic surfaces, it is vital to study the recovery process of the gas–liquid interface in addition to methods of enhancing the stability of the gas–liquid interface. By installing electrodes at the bottom of a microstructure, Lee and Kim[26] realized the automatic recovery of the gas–liquid interface. The principle is that when the microstructure is immersed in water, the electrodes are connected and the gas generated by the electrolysis of water restores the gas–liquid interface. The interface returns to the Cassie state when the water leaves the bottom of the microstructure, because the electrodes are disconnected, and the process of electrolysis of water is automatically terminated. Inspired by the Salvinia leaf in nature, Xiang *et al.*[27] studied the effects of bottom wedge-shaped grooves, middle hair stems, and top eggbeater-shaped hair heads on the recovery and regulation of the air layer.

Building on previous research results, this paper describes the design of a new composite structure on the surface of microchannels that combines a reentrant structure with a transverse post. The reentrant structure contains primary and doubly reentrant structures, which are then combined into primary reentrant post structures and doubly reentrant post structures. Experiments have demonstrated that this composite structure greatly enhances the gas–liquid interface stability, and the length of the grooves transitions from the micrometer level to the millimeter scale through the regular arrangement of the posts. In addition, the mechanism of interface collapse in the micro-ridge structures and the reasons for the interface being maintained by the new composite structures are analyzed through numerical simulations. We also study the factors affecting the stability of the gas–liquid interface to provide guidance for structural optimization.

II. RESEARCH METHODOLOGY

A. Experimental setup

The experimental device is shown in Fig. 1. The experimental platform is based on an inverted microscopic platform (ZEISS, Axio Observer, Germany), with a 10× objective lens (ZEISS, EC Plan-NEOFLUAR, Germany) used to observe the flow in the microchannel. The microchannel was manufactured by 3D printing and fixed to the stage of the microscope. One side of the microchannel is connected to the injection pump (Suzhou Xunfei, XF-102PD, China), and deionized water is injected into the channel at a stable flow rate through the injection pump. The other side of the microchannel is connected to the beaker by a liquid recovery tube. To achieve the lighting intensity required for high-speed camera shooting, LED lights are positioned above the microchannel, and a translucent plate is installed on the LED lights to further improve the image shooting quality. A high-speed camera (Phantom, VEO 710L, America) controlled by the computer is used to obtain the images. In the experiments, the sampling frame covered $1152 \times 320\,\text{pixels}^2$, the sampling frequency was 4000 fps, and the longest single sampling time was 32 s.

The microchannel used in the experiment was independently designed and processed by the nanoArch S130 printing system (Shenzhen Mofang Material Technology Co., Ltd., China). The printing accuracy of this device is 2 μm, and the minimum layer thickness is 5 μm, which satisfy the machining accuracy requirements for the experiments. The 3D printing material was a semi-transparent photosensitive resin, which has sufficient material strength and transparency: Its tensile strength is 80 MPa, and its elastic modulus is 4.5 GPa, satisfying the experimental requirements for channel strength and deformation resistance. As shown in Fig. 2, the contact angle of deionized water on the solidified plane made of photosensitive resin is $53.9° \pm 2.9°$, as measured by a contact angle measurement instrument

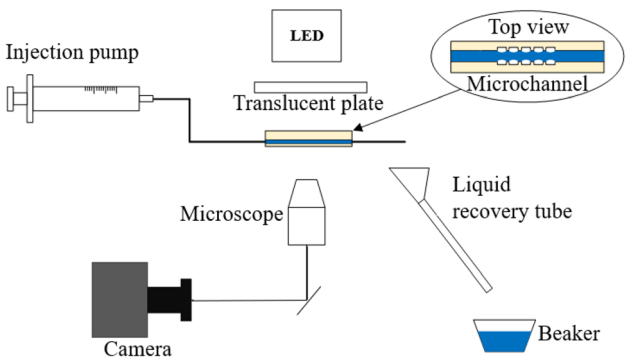

FIG. 1. Schematic diagram of experimental device.

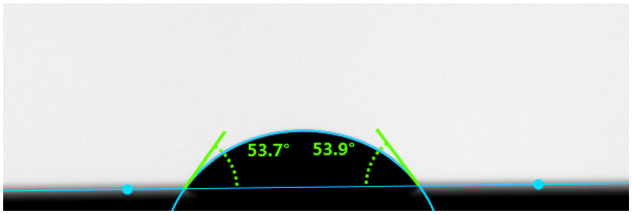

FIG. 2. Contact angle measurement results of a 3D printed flat plate.

(DataPhysics, OCA 25, Germany). This indicates that the microchannel surface manufactured by 3 D printing is hydrophilic.

To observe the effect of different structures on maintaining the gas–liquid interface, we designed two major structures: a common surface groove structure (SGS) and a specially designed transverse post structure (TPS). Each of these was further divided into three types based on the condition of the groove sidewall: no reentrant structure (NR), primary reentrant structure (PR), and doubly reentrant structure (DR). The 3D printing used the stitching mode to achieve a printing size of 38.4 mm (length) × 21.6 mm (width) × 10 mm (height). Six different microchannel structures were processed simultaneously on the same microchannel integrated system, thus ensuring the same machining accuracy for each microchannel and greatly reducing the processing time. As shown in Fig. 3, the final processed microchannel integration system contains six microchannels with different structures: NR-TPS, PR-TPS, DR-TPS, NR-SGS, PR-SGS, and DR-SGS. The 3 D printing system integrates the processing of microchannel interfaces, which are circular holes with a diameter of 0.7 mm and a depth of 5 mm. A stainless steel pipe with an outer diameter of 0.65 mm was inserted into the hole and sealed with glue to facilitate the connection of an external capillary tube. The dimensions of the microchannel structure, shown in Fig. 4, are $L = 200\ \mu$m, $H = 160\ \mu$m, $D = 80\ \mu$m, $S = 60\ \mu$m, $w = 15\ \mu$m, and $h = 10\ \mu$m. Figures 4(a) and 4(d) show schematic diagrams of the NR-TPS and NR-SGS microchannels, while Figs. 4(b) and 4(e) and Figs. 4(c) and 4(f) show partial schematic diagrams of the primary and doubly reentrant structures, respectively. The corresponding dimensions of the reentrant structures are $D_1 = 70\ \mu$m, $D_2 = 20\ \mu$m, and $w_1 = 10\mu$m; the remaining dimensions are consistent with the NR structures.

B. Numerical simulations

As a mesoscopic method, the LBM has attracted widespread attention in recent years due to its simple boundary treatment, easy programmatic implementation, and good parallel performance.[28–32] This method was developed on the basis of a lattice gas cellular automaton models,[33] since when a variety of models have been developed. For multiphase flows, according to the different methods of dealing with interactions, the common approaches can be roughly divided into four categories:[34] color-gradient models,[35] pseudopotential models,[36] free-energy models,[37] and kinetic models.[38] We use a multicomponent multiphase (MCMP) model[39] in this study, which is a pseudopotential model.

The gas–liquid two-phase flow system can be regarded as being composed of two components: water (component 1) and air (component 2). Each component has its corresponding particle distribution function,[40]

$$f_\alpha^\sigma(\vec{r}+\vec{e}_\alpha\Delta t, t+\Delta t) - f_\alpha^\sigma(\vec{r},t) = \frac{1}{\tau^\sigma}\left[f_\alpha^{\sigma(eq)}(\vec{r},t) - f_\alpha^\sigma(\vec{r},t)\right], \quad \sigma = 1,2, \tag{1}$$

where $f_\alpha^\sigma(\vec{r},t)$ is the density distribution function of component σ at lattice site $\vec{r}$ and time t, $f_\alpha^{\sigma(eq)}$ is the equilibrium distribution function, and τ^σ is the dimensionless relaxation time, which represents the average time interval between two physical collisions. The viscosity in the lattice unit is related to the collision time according to $\nu^\sigma = c_s^2\left(\tau^\sigma - \frac{1}{2}\right)\Delta t$, where c_s is the lattice speed and $c_s^2 = \frac{1}{3}$.

The equilibrium distribution function $f_\alpha^{\sigma(eq)}$ has the following form:

$$f_\alpha^{\sigma(eq)} = \rho_\sigma\omega_\alpha\left[1 + \frac{\vec{e}_\alpha\cdot\vec{u}^{\sigma(eq)}}{c_s^2} + \frac{\left(\vec{e}_\alpha\cdot\vec{u}^{\sigma(eq)}\right)^2}{c_s^4} - \frac{\left(\vec{u}^{\sigma(eq)}\right)^2}{2c_s^2}\right]. \tag{2}$$

For the D3Q19 model[41] with 19 velocity directions at a given point in three-dimensional space, the weight factors are given by

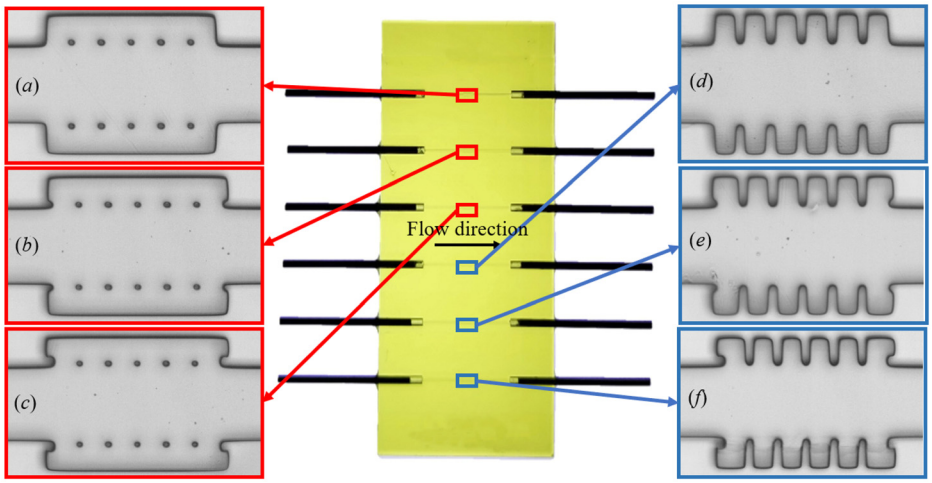

FIG. 3. Physical diagram of the microchannel integrated system. The box shows a partial enlarged view of the microchannel structure: The red box on the left shows the TPS: (a) NR-TPS, (b) PR-TPS, and (c) DR-TPS. The blue box on the right side shows the SGS: (d) NR-SGS, (e) PR-SGS, and (f) DR-SGS.

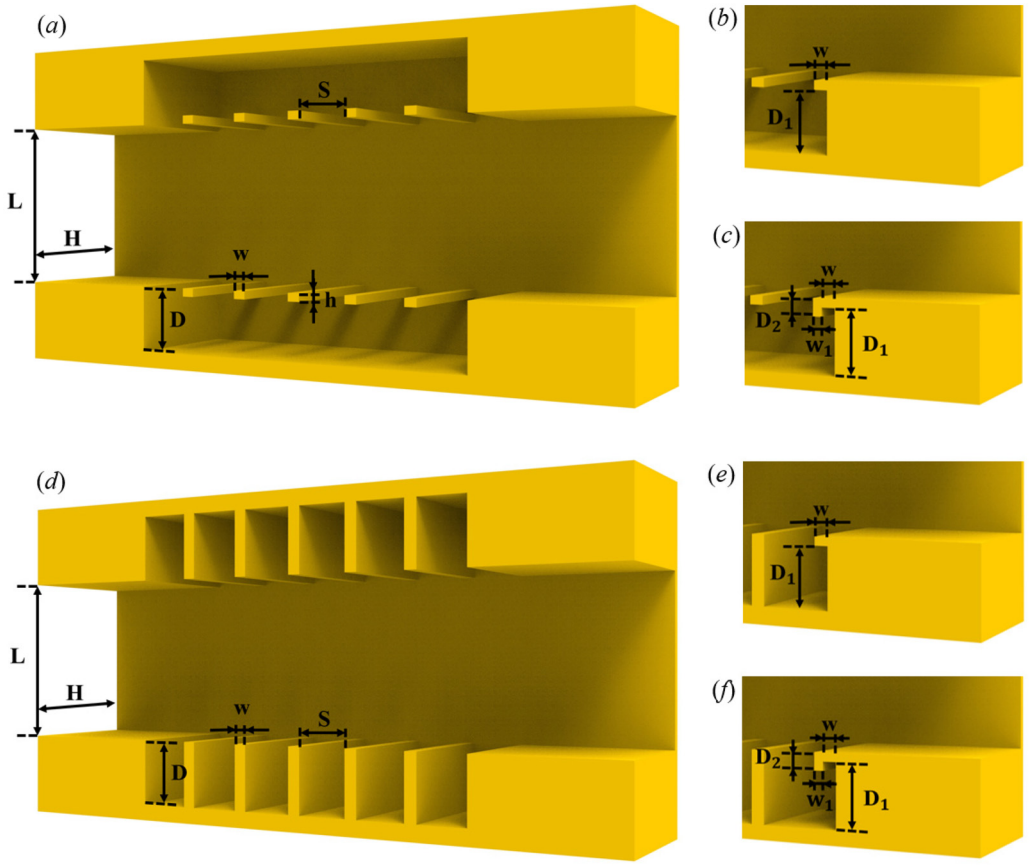

FIG. 4. Schematic diagram of microchannel structure dimensions. (a) and (d) NR-TPS and NR-SGS, respectively. (b) and (e) A partial schematic diagram of the primary reentrant structure on the outlet side. (c) and (f) A partial schematic diagram of the doubly reentrant structure on the outlet side. The remaining structural dimensions are consistent with the NR structures.

$$\omega_\alpha = \begin{cases} \frac{1}{3}, & \alpha = 0 \\ \frac{1}{18}, & \alpha = 1-6 \\ \frac{1}{36}, & \alpha = 7-18. \end{cases} \tag{3}$$

The fluid density and velocity can be obtained from the statistical moments of the density distribution functions, $\rho^\sigma = \sum_{\alpha=0}^{18} f_\alpha^\sigma$, $\vec{u}^\sigma = \frac{1}{\rho^\sigma}\sum_{\alpha=0}^{18}(f_\alpha^\sigma \cdot \vec{e}_\alpha)$.

In Shan and Chen's MCMP pseudopotential model, the interaction forces between fluids can be divided into the intramolecular interaction $\vec{F}_{\sigma\sigma}$ between the same component and the intermolecular interaction $\vec{F}_{\sigma\bar{\sigma}}$ between different components,[42]

$$\vec{F}_{\sigma\sigma}(\vec{r},t) = -G_{\sigma\sigma}\psi^\sigma(\vec{r},t)\sum_{\alpha=1}^{18} w(|\vec{e}_\alpha|^2)\psi^{\bar{\sigma}}(\vec{r}+\vec{e}_\alpha\delta_t,t)\vec{e}_\alpha, \tag{4}$$

$$\vec{F}_{\sigma\bar{\sigma}}(\vec{r},t) = -G_{\sigma\bar{\sigma}}\psi^\sigma(\vec{r},t)\sum_{\alpha=1}^{18} w(|\vec{e}_\alpha|^2)\psi^{\bar{\sigma}}(\vec{r}+\vec{e}_\alpha\delta_t,t)\vec{e}_\alpha, \tag{5}$$

$$\vec{F}_{\bar{\sigma}\sigma}(\vec{r},t) = -G_{\bar{\sigma}\sigma}\psi^{\bar{\sigma}}(\vec{r},t)\sum_{\alpha=1}^{18} w(|\vec{e}_\alpha|^2)\psi^{\sigma}(\vec{r}+\vec{e}_\alpha\delta_t,t)\vec{e}_\alpha, \tag{6}$$

where $G_{\sigma\sigma}$ reflects the interaction strength between the same component, $G_{\sigma\bar{\sigma}}$ and $G_{\bar{\sigma}\sigma}$ reflect the interaction strength between different components ($G_{\sigma\bar{\sigma}} = G_{\bar{\sigma}\sigma}$), and $w(|\vec{e}_\alpha|^2)$ are the weight factors, where $w(1) = 1/6$ and $w(2) = 1/12$. The different components have different interaction potential functions as follows: $\psi^\sigma(\vec{r},t) = \rho^\sigma(\vec{r},t)$, $\psi^{\bar{\sigma}}(\vec{r},t) = \rho^{\bar{\sigma}}(\vec{r},t)$.

The interaction between fluids affects the equilibrium velocity $\vec{u}^{\sigma(eq)}$ according to

$$\vec{u}^{\sigma(eq)} = \vec{u}' + \frac{\tau^\sigma(\vec{F}_{\sigma\sigma}+\vec{F}_{\sigma\bar{\sigma}})}{\rho^\sigma}, \tag{7}$$

where $\vec{u}'$ is the common velocity defined by the law of conservation of momentum,

$$\vec{u}' = \frac{\sum_\sigma\left(\frac{\rho^\sigma\vec{u}^\sigma}{\tau^\sigma}\right)}{\sum_\sigma\left(\frac{\rho^\sigma}{\tau^\sigma}\right)}. \tag{8}$$

Finally, the actual physical velocity $\vec{u}_r$ is the average velocity before and after the collision, which is given by

$$\vec{u}_r = \frac{\sum_\sigma \rho^\sigma \vec{u}^\sigma + \frac{\Delta t}{2}\sum_\sigma \vec{F}_\sigma}{\sum_\sigma \rho^\sigma}. \tag{9}$$

The pressure is calculated by the following equation:

$$p = c_s^2 \sum_\sigma \rho^\sigma + \frac{1}{2}c_s^2 \sum_\sigma G_{\sigma\sigma}\left[\psi^\sigma(\vec{r})\right]^2 + \frac{1}{2}c_s^2 \sum_{\sigma\neq\bar{\sigma}} G_{\sigma\bar{\sigma}}\psi^\sigma(\vec{r})\psi^{\bar{\sigma}}(\vec{r}). \tag{10}$$

III. RESULTS AND DISCUSSION

A. Analysis of flow phenomena

Ou and Rothstein[2] demonstrated experimentally that a stable gas–liquid interface can be formed on a hydrophobic surface with a microgroove. However, it is difficult to form a stable gas–liquid interface on a hydrophilic surface with a microgroove. Figure 5(a) illustrates the formation and maintenance of a gas–liquid interface in hydrophilic groove structures in our experiments. The groove areas (circled in red) have been completely wetted by water and cannot form a stable gas–liquid interface in the NR-SGS case. Zhang *et al.*[24] successfully formed a gas–liquid interface in a hydrophilic microchannel by adding doubly reentrant structures to the sidewall of the microgrooves. However, these doubly reentrant structures increase the processing complexity. Therefore, in our experiments, the doubly reentrant structures are only placed on the inlet and outlet of the sidewall to explore the effect on maintaining the stability of the gas–liquid interface. As shown in Figs. 5(b) and 5(c), some grooves are still completely saturated with water, and a stable gas–liquid interface cannot be formed in the PR-SGS and DR-SGS cases. We explore the reasons for this using numerical simulations.

By adapting Shan and Chen's MCMP model, we achieved a flow process in the PR-SGS case. As shown in Fig. 6, the dark-blue curved surface represents the gas–liquid interface, the black arrows on the interface represent the velocity vectors, the light-blue area represents the gas phase, and the gray area represents the solid wall. Figures 6(a)–6(c) show the process of liquid entering the groove in sequence, and panels (a1)–(c1) show locally enlarged views of the collapsed interface. The numerical simulation results indicate that some grooves in the PR-SGS case have been wetted by liquid. The velocity vectors show that, owing to the hydrophilic nature of the solid wall, there is an adsorption force acting on the liquid that gradually "pulls" the liquid into the grooves along the wall, resulting in the instability of the gas–liquid interface and the grooves being wetted by the liquid. As shown in the yellow boxes in Figs. 6(a1) and 6(b1), the liquid has a large velocity near the solid wall, indicating that the hydrophilic wall imposes a great adsorption force on the liquid.

Based on this result, we propose the bold idea that cutting off the infiltrating passage along the solid wall toward the bottom of the groove, while also providing pinning points for the liquid during the flow process, may enhance the ability of the microchannel to maintain a stable gas–liquid interface. Thus, we modify the microstructure by cutting off the bottom part of the groove and retaining only a small top section to provide a pinning point for the liquid. This is the TPS shown in Figs. 4(a)–4(c). When simulating the flow process in PR-TPS, the channel size and liquid flow rate at the inlet remain the same as those in the PR-SGS case described above. The simulation results in Fig. 7 show that the TPS maintains the gas–liquid interface very well. When the liquid touches the post, it rapidly expands along the prism of the post. The liquid has a large velocity near the prism, as shown in Fig. 7(a1). Because the passage by which the liquid infiltrates along the wall toward the bottom of the groove has been cut off, the liquid no longer continues to infiltrate into the groove, but is firmly fixed to the post. When the gas–liquid interface forms on both sides of the post, it creates a "pulling force" toward the middle of the interface because of its hydrophilic nature, further helping the interface to maintain stability, as shown in the yellow boxes in Figs. 7(b1) and 7(c1).

The simulation results have already shown that the TPS greatly improves the interface stability over that of the SGS. This is now

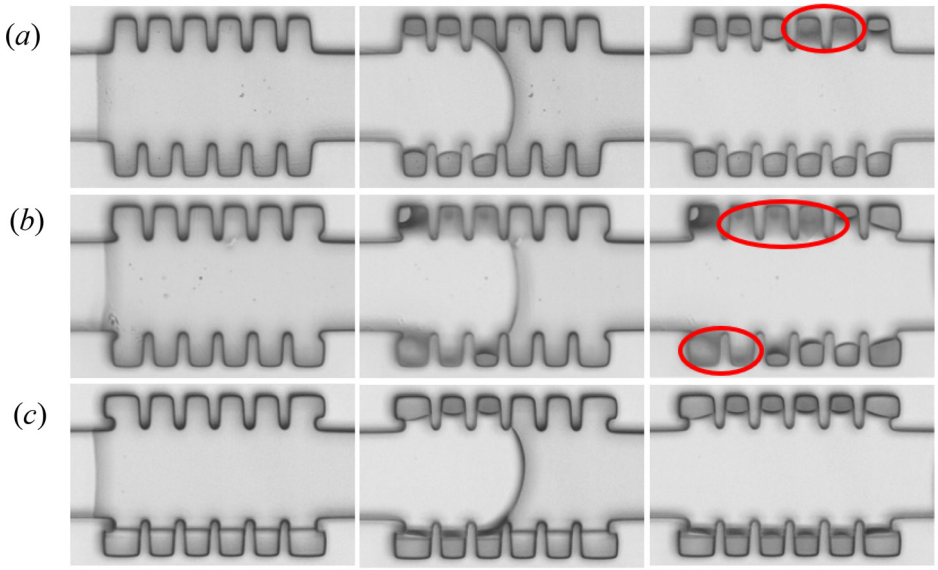

FIG. 5. Formation and maintenance of gas–liquid interface in microchannels with different structures: (a) NR-SGS, (b) PR-SGS, and (c) DR-SGS. The flow rate of the de-ionized water and the sampling frequency of the camera are the same for the different structures.

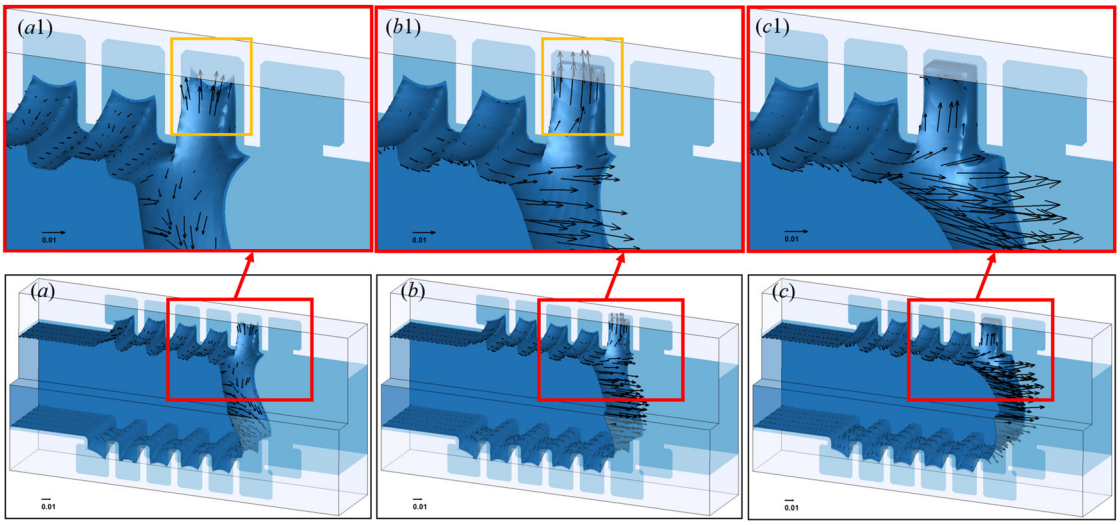

FIG. 6. Collapse process of gas–liquid interface in PR-SGS. (a)–(c) The process of water entering the groove and (a1)–(c1) partial enlarged images of (a)–(c), respectively.

further verified by experiments. As shown in Figs. 4(a)–4(c), three kinds of TPS were processed by 3 D printing to give the NR-TPS, PR-TPS, and DR-TPS. The flow rate of the de-ionized water and the sampling frequency of the camera in the TPS cases remain the same as those in the SGS experiments. The experimental results are shown in Fig. 8. Compared with the structures in Figs. 5(a)–5(c), the only changes are from grooves to posts; all other structures and dimensions remain unchanged. The NR-TPS in Fig. 8(a) has been completely saturated with liquid, while in Figs. 8(b) and 8(c), continuous and stable gas–liquid interfaces are formed in both the PR-TPS and DR-TPS cases. As shown in Fig. 8(a), the liquid begins to infiltrate along the sidewall at the entrance of the groove, so that the entire groove is completely saturated with liquid. However, the reentrant structure in Figs. 8(b) and 8(c) effectively inhibits the infiltration of the liquid along the sidewall to the bottom of the groove by providing pinning points for the gas–liquid interface at the inlet, thus contributing to the formation of the gas–liquid interface.

As shown in Fig. 9, the interface remains stable even when the number of posts is increased, and the length of the gas–liquid interface can reach 1185 μm. Therefore, we have effectively improved the gas–liquid interface stability through a composite structure that combines a transverse post and reentrant structures. This composite structure

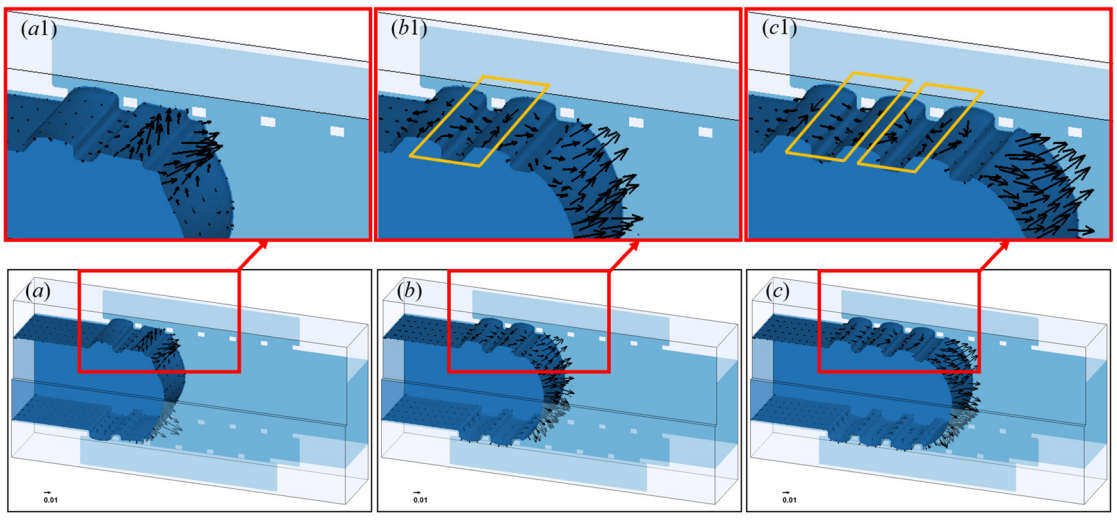

FIG. 7. Evolution of gas–liquid interface in PR-TPS. (a)–(c) The process of water flowing through the microstructures and (a1)–(c1) partial enlarged images of (a)–(c), respectively.

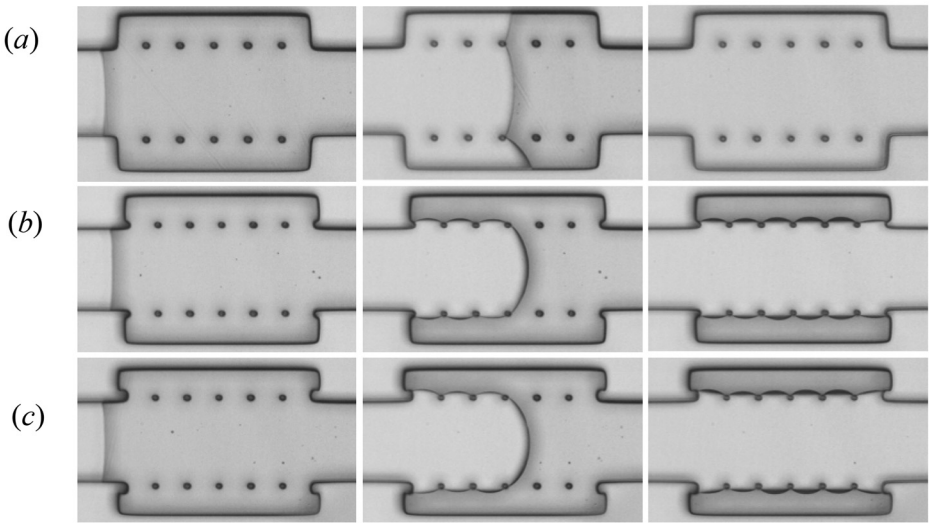

FIG. 8. Formation and maintenance of gas–liquid interface in microchannels with different structures. (a) NR-TPS, (b) PR-TPS, and (c) DR-TPS. The flow rate of the de-ionized water and the sampling frequency of the camera are the same for the different structures.

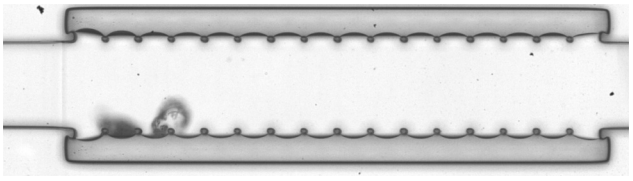

FIG. 9. Gas–liquid interface reaches a length of 1185 μm.

not only helps to form stable gas–liquid interfaces in hydrophilic microchannels, but also increases the stable size of the gas–liquid interface from the micrometer level to the millimeter scale.

In summary, through experiments and simulations, we have found that the liquid in the SGS could infiltrate along the solid wall to the bottom of the groove because of the hydrophilic nature of the surface, ultimately causing the gas–liquid interface to collapse. Therefore, based on this instability mechanism, we designed a composite structure combining a transverse post and a reentrant structure. The transverse post cuts off the infiltrating passage to the bottom of the groove and provides a pinning point for the liquid, effectively maintaining interface stability. The ability of the composite structure to maintain the gas–liquid interface has been verified through both experiments and simulations.

B. Two different collapse types caused by two different inlet structures

Compared with the traditional groove structure, the composite structure combining a transverse post and a reentrant structure designed in this study greatly enhances the ability to maintain a stable gas–liquid interface. However, the interface will still collapse when the Reynolds number *Re* becomes large or the spacing between the posts is increased. Our research indicates that there are two different collapse types caused by two of the inlet structures, namely, PR-TPS and DR-TPS. The interface begins to collapse from the edge of the sidewall in the PR-TPS case, while the collapse is initiated at the edge of the post in the DR-TPS case.

As shown in Fig. 10, surface tension acts upward to balance the pressure difference and thus maintain the stability of the interface. The critical pressure difference can be estimated by the Laplace equation: $\Delta p = \frac{2T\sin\theta_b}{Sl} = \frac{2\gamma\sin\theta_b}{S}$, where T is the surface tension, θ_b is the equilibrium contact angle, l is the length of the contact line, and S is the spacing of the structure. If the equilibrium contact angles of the primary reentrant structure and doubly reentrant structure are θ_1 and θ_2, respectively, the corresponding critical pressure differences are $\Delta p_{c1} = \frac{2\gamma\sin\theta_1}{S}$ and $\Delta p_{c2} = \frac{2\gamma\sin\theta_2}{S}$. According to Zhang *et al.*,[24] Δp_{c1} is less than Δp_{c2} because θ_1 is less than θ_2. When the structures on either side of the interface are symmetrical, the equilibrium contact angle is the same on both sides of the interface, as shown in Figs. 10(a) and 10(b). When the structures on either side of the interface are asymmetrical, the equilibrium contact angles are not equal, as shown in Fig. 10(c), and take values of $\theta_2 + \theta$ and $\theta_1 - \theta$, respectively.

The collapse processes of the gas–liquid interface in the PR-TPS case are shown in Figs. 11(a)–11(f); panels (a1)–(c1) are partial enlarged images of panels (a)–(c), respectively. For the PR-TPS case, when the pressure difference across the gas–liquid interface is greater than the critical pressure difference, the gas–liquid interface cannot maintain its curvature while also keeping the contact line pinned. Thus, the interface begins to collapse. In Fig. 11(a1), the pressure at upstream position 1 is slightly higher than that at downstream position 2. The pressure at position 1 reaches the critical pressure first, and the interface begins to collapse from position 1. The two-phase contact line at position 1 gradually slides toward the reentrant sidewall, as shown by the red arrow in Fig. 11(a1). When the interface contacts the vertical sidewall, it quickly slides along the sidewall toward the bottom of the groove, as shown by the red arrows in Figs. 11(b1) and 11(c1). When the interface contacts the bottom of the groove, it moves forward along the bottom wall until the liquid completely infiltrates the entire groove.

For the DR-TPS case, as shown in Fig. 12, the critical pressure at upstream position 3 is Δp_{c2} and the critical pressure at downstream

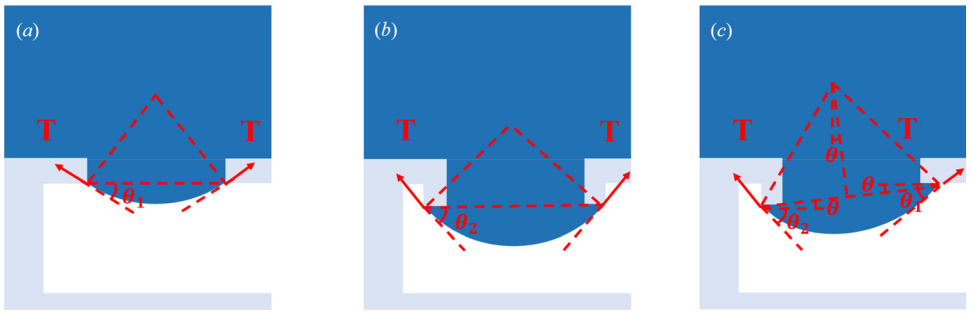

FIG. 10. Schematic diagrams illustrating the gas–liquid interface between different structures: (a) Primary reentrant structure on the left and transverse post structure on the right. (b) Doubly reentrant structures on both sides. (c) Doubly reentrant structure on the left and transverse post structure on the right.

position 4 is Δp_{c1}. According to Zhang *et al.*,[24] Δp_{c1} is less than Δp_{c2}, so the pressure at position 4 reaches the critical pressure first and the interface begins to collapse from position 4. As shown by the red arrow in Fig. 12(a1), the interface on either sides of the post moves toward the middle, touches, and fuses, forming a complete interface. As a part of the interface is still pinned to the post, the interface exhibits an "m" shape, as shown in Fig. 12(b1). Subsequently, the entire interface detaches from the post and exhibits a "c" shape, as shown in Fig. 12(c1).

C. Factors influencing the stability of the gas–liquid interface in TPS

Previous studies have found that a smaller solid fraction $w/(w+S)$ of superhydrophobic surfaces produces a better drag reduction effect. If the post width w is unchanged, a larger post spacing S will, therefore, generate improved drag reduction. However, a larger S also means that the interface is more prone to collapse at high *Re*. Therefore, it is necessary to study the critical relationship between the post spacing S and *Re*, which will assist in the design of the optimal structure size for different flow situations in practical applications.

We use numerical simulations to explore the critical relationship between S and *Re*. This not only allows us to flexibly set the structure parameter S and flow parameter *Re*, but also prevents environmental factors from impacting the results. According to the analysis in the appendix, we use the medium-resolution grid to simulate various flow cases. The initial state and structure sizes are consistent with the description in the Appendix.

Figures 13(a) and 13(b) represent the gas–liquid interface formation and maintenance for various S and *Re* in the PR-TPS and DR-TPS cases. The horizontal coordinate is *Re*, and the vertical coordinate

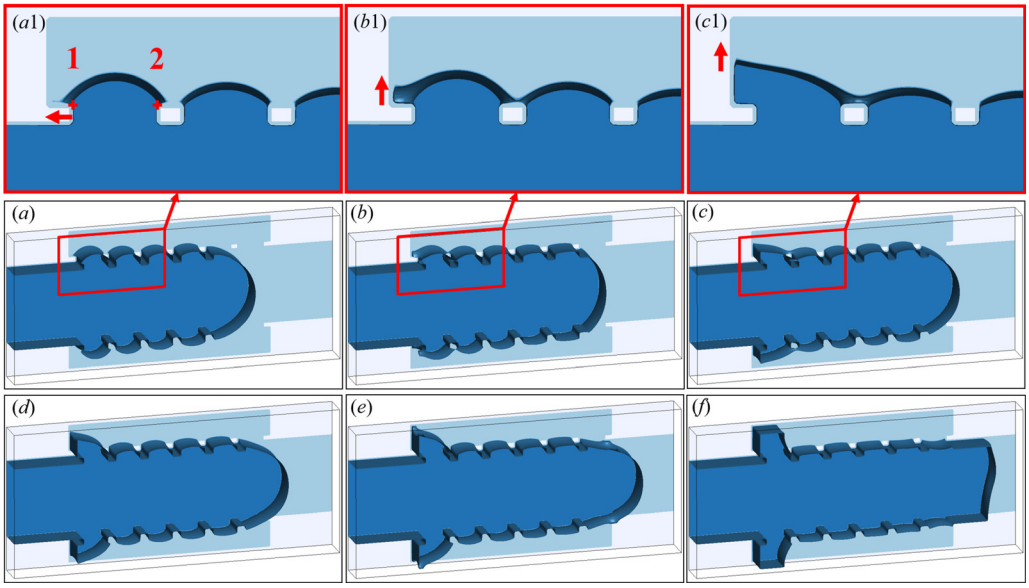

FIG. 11. Collapse process of the gas–liquid interface in PR-TPS. (a)–(f) The collapse process of the gas–liquid interface in sequence. The dark-blue curved surface represents the gas–liquid interface, the light-blue area represents the gas phase, and the white area represents the solid wall; (a1)–(c1) partial enlarged images of (a)–(c), respectively.

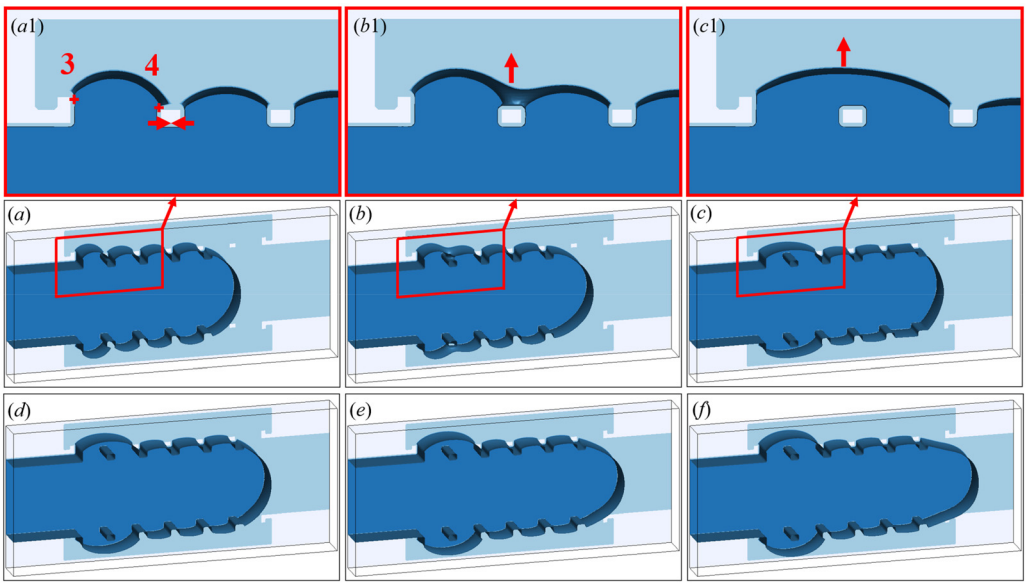

FIG. 12. Collapse process of the gas–liquid interface in DR-TPS. (a)–(f) The collapse process of the gas–liquid interface in sequence. The dark-blue curved surface represents the gas–liquid interface, the light-blue area represents the gas phase, and the white area represents the solid wall; (a1)–(c1) partial enlarged images of (a)–(c), respectively.

is the dimensionless column spacing S/D. The black dots indicate that the gas–liquid interface can be formed and stably maintained under the corresponding S/D and Re. The red crosses denote that the gas–liquid interface is unstable and the groove will be completely infiltrated by liquid under the corresponding S/D and Re. As Re increases, the spacing S that can maintain a stable interface decreases. After fitting, the critical functional relation between S/D and Re is obtained as $\frac{S}{D} = 1.530\mathrm{Re}^{-0.3562}$.

Comparing the flow phase diagrams in the PR-TPS and DR-TPS cases, it is apparent that the DR-TPS cannot maintain the gas–liquid interface as effectively as the PR-TPS when $Re = 2.6175$, $S/D = 1.0$, and $Re = 6.9$, $S/D = 0.7$, which conflicts with the original design intention. As shown in Fig. 10(c), when the structures on either side of the interface are asymmetrical, the contact angles on each side are unequal, with an upstream contact angle of $\theta_2 + \theta$ and a downstream contact angle of $\theta_1 - \theta$. Because $\theta_1 < \theta_2$, the critical pressure difference for the DR-TPS is determined by the downstream contact angle $\theta_1 - \theta$. Thus, the critical pressure $\Delta p_{DR-TPS} = \frac{2\gamma \sin(\theta_1 - \theta)}{S}$ is less than $\Delta p_{PR-TPS} = \frac{2\gamma \sin\theta_1}{S}$, which explains why the PR-TPS cannot maintain interface stability as well as the DR-TPS.

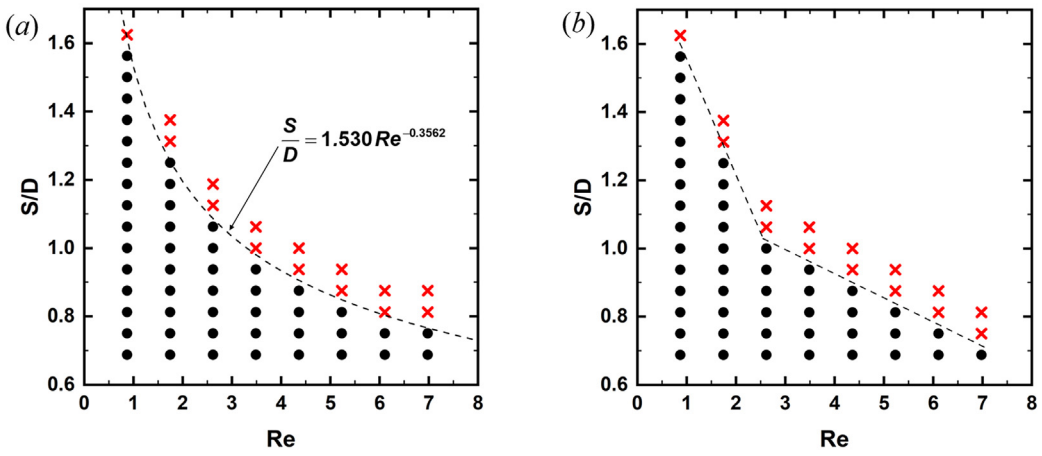

FIG. 13. Gas–liquid interface formation and maintenance situation. Black dots indicate that the gas–liquid interface can be formed and stably maintained under the corresponding S/D and Re. Red crosses denote that the gas–liquid interface is unstable and the groove will be completely infiltrated by liquid under the corresponding S/D and Re. (a) Flow phase diagram for PR-TPS. (b) Flow phase diagram for DR-TPS.

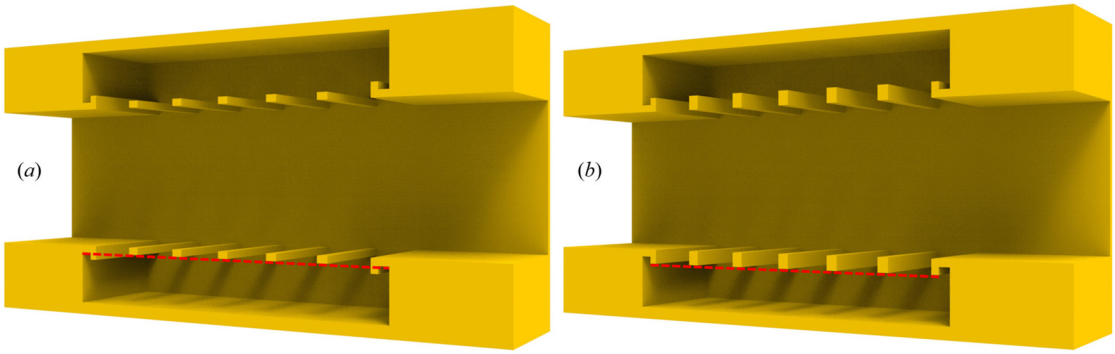

FIG. 14. Schematic diagram of the DR-TPS before and after improvement. (a) DR-TPS and (b) OPTI-DR-TPS.

Based on this analysis, we further improve the DR-TPS. As shown in Fig. 14, increasing the thickness of the post to keep it in line with the undersurface of the doubly reentrant structure eliminates the reduction in the downstream contact angle caused by the tilted interface. Thus, the critical pressure difference effectively improves, and the ability of the structure to maintain a stable interface is enhanced. We now focus on this optimized DR-TPS (OPTI-DR-TPS).

We traced the pressures p_{in} and p_{out} on both sides of the gas–liquid interface and obtained the curves of the pressure difference Δp across the interface over time under the conditions of $Re = 6.98$, $S/D = 1.17$, and $w = 3$. The gas–liquid interfaces in three structures all eventually become unstable under these conditions. As shown in Fig. 15(a), during the liquid flow process, there are small oscillations at the interface every time the liquid passes a post. For the DR-TPS, Δp reaches its maximum value when $t = 12000$ and then declines. Based on the morphology of the gas–liquid interface in Fig. 15(b), it can be observed that the gas–liquid interface has already become unstable when $t = 12000$. Therefore, it can be considered that the pressure difference at this time is the maximum pressure difference that the DR-TPS structure can withstand, denoted as $\Delta p_{DR-TPS} = 0.0119$. Similarly, we obtain the critical pressure difference of the other two structures, $\Delta p_{DR-TPS} = 0.0128$ and $\Delta p_{DR-TPS} = 0.0133$. Comparing the critical pressure differences of these three structures, $\Delta p_{DR-TPS} < \Delta p_{PR-TPS} < \Delta p_{OPTI-DR-TPS}$, which is consistent with the theoretical analysis above.

We simulated the OPTI-DR-TPS under different S/D and Re to obtain the flow phase diagrams shown in Fig. 16(a). The red dashed line indicates the division between whether the interface remains stable in the PR-TPS, and the black dashed line denotes the division between whether the interface remains stable in the OPTI-DR-TPS. Clearly, the ability to maintain a stable interface is greatly enhanced in the OPTI-DR-TPS case. The critical relationships between S/D and Re obtained through fitting are $\frac{S}{D} = 1.530\mathrm{Re}^{-0.3562}$ for PR-TPS and $\frac{S}{D} = 1.619\mathrm{Re}^{-0.3126}$ for OPTI-DR-TPS. As Re increases, S/D decreases more slowly in OPTI-DR-TPS. We verified these expressions through a series of experiments. Figures 16(b) and 16(c) show the interface situation in the DR-TPS and OPTI-DR-TPS cases under the same flow rate: Panel (b) corresponds to the original DR-TPS, and panel (c) corresponds to the improved OPTI-DR-TPS. By adjusting the thickness of the post, the ability of the DR-TPS to maintain the gas–liquid interface has been successfully enhanced. In our experiments, the gas–liquid interface survives more than 30 min in OPTI-DR-TPS under the conditions of $Re = 6.98$, $S/D = 1$, and $w = 3$.

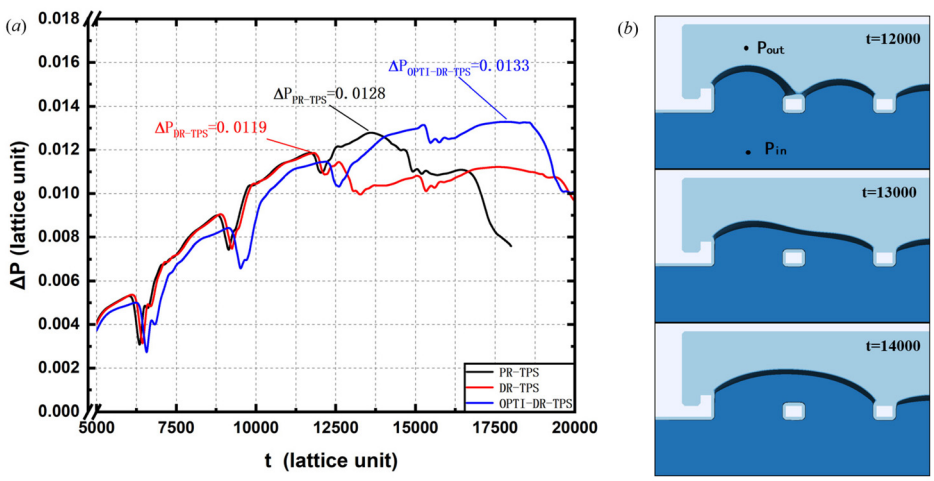

FIG. 15. (a) Pressure difference curves for PR-TPS, DR-TPS, and OPTI-DR-TPS under the condition of $Re = 6.98$, $S/D = 1.17$, and $w = 3$. (b) Interface morphology of DP-TPS.

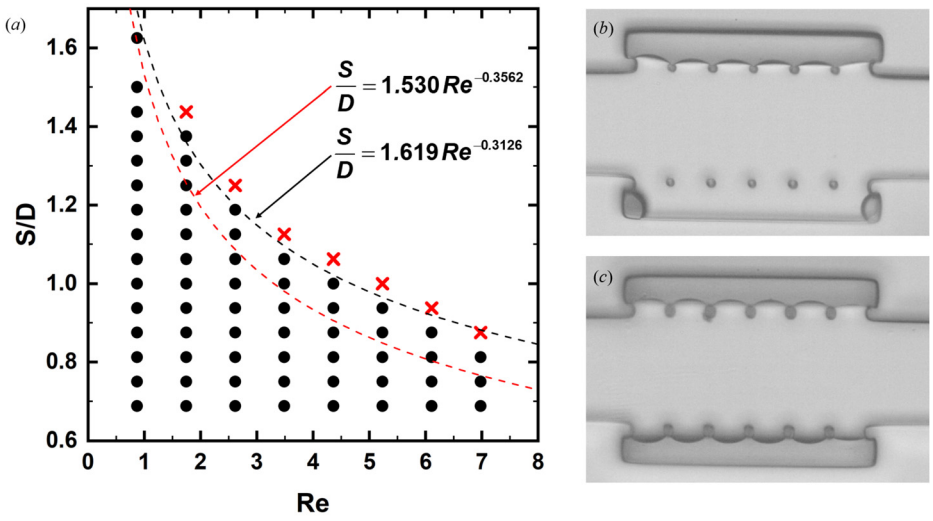

FIG. 16. Ability of the DR-TPS to maintain the gas–liquid interface has been successfully enhanced. (a) Flow phase diagrams of OPTI-DR-TPS under different *S*/*D* and *Re*. The black dots indicate that the gas–liquid interface can be formed and stably maintained under the corresponding *S*/*D* and *Re*. The red crosses denote that the gas–liquid interface is unstable and the groove will be completely infiltrated by liquid under the corresponding *S*/*D* and *Re*. The red dashed line is the dividing line between whether the interface can be stably maintained by the PR-TPS, and the black dashed line is the dividing line between whether the interface can be stably maintained by the OPTI-DR-TPS. (b) Interface situation of the DR-TPS at a flow rate of 75 μl/min. The gas–liquid interface on one side has completely collapsed, and the liquid has entered the groove. (c) Interface situation of the OPTI-DR-TPS at a flow rate of 75 μl/min. The gas–liquid interfaces on both sides remain stable during continuous liquid flow.

Our studies have proved that the OPTI-DR-TPS has the strongest ability to maintain the gas–liquid interface. Thus, we further explore the influence of the post width *w* on the stability of the gas–liquid interface based on the OPTI-DR-TPS. As shown in Fig. 17, the dividing line between whether the interface can be stably maintained

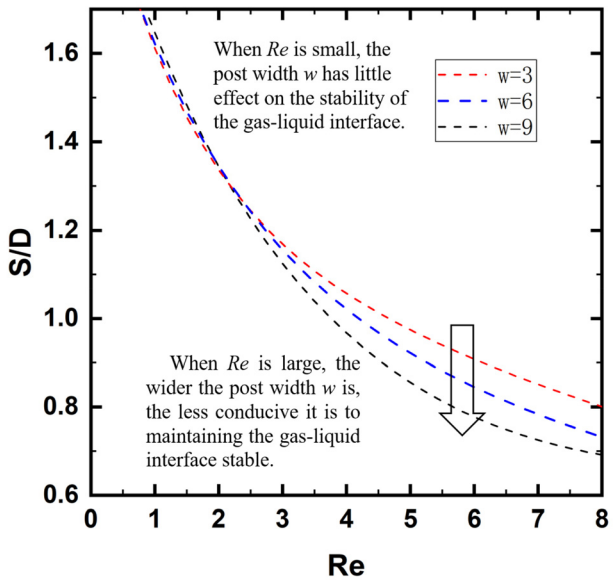

FIG. 17. Dividing line between whether the interface can be stably maintained under different post widths *w*.

was obtained under different values of *w* through a series of simulations. When *Re* is small, *w* has little effect on the stability of the gas–liquid interface, and the three profiles almost overlap. When *Re* is large, the spacing *S* between the posts required to maintain interface stability at the same *Re* decreases as the post width *w* increases. This indicates that wider posts are less conducive to maintaining a stable gas–liquid interface.

We traced the pressures p_{in} and p_{out} on either side of the gas–liquid interface and obtained the profiles of the pressure difference Δp across the interface over time. As shown in Fig. 18(a), Δp exhibits periodic fluctuations. The interface morphologies at the peaks of Fig. 18(a) are shown in Fig. 18(b). During the liquid flow process, there are small oscillations at the interface every time the liquid passes a post. When *Re* is small, the post width *w* has little effect on the amplitude of the interface oscillations. As shown in Fig. 18(a), when $Re = 1.745$, the maximum amplitudes of the three profiles do not differ significantly. However, the influence of *w* on the amplitude of interface oscillations increases as *Re* increases. When $Re = 5.235$, the maximum amplitude with $w = 9$ is much greater than that when $w = 3$. A larger post width *w* produces a greater amplitude of interface oscillation and makes interface collapse more likely. Therefore, wider posts are less conducive to maintaining a stable gas–liquid interface. Overall, when *Re* is small, the post width *w* has little effect on interface stability. When *Re* is large, wider post widths result in a less stable gas–liquid interface.

IV. CONCLUSIONS

This paper has described a class of composite structures combining transverse posts and reentrant structures in microchannels. The formation and maintenance of the gas–liquid interface in the

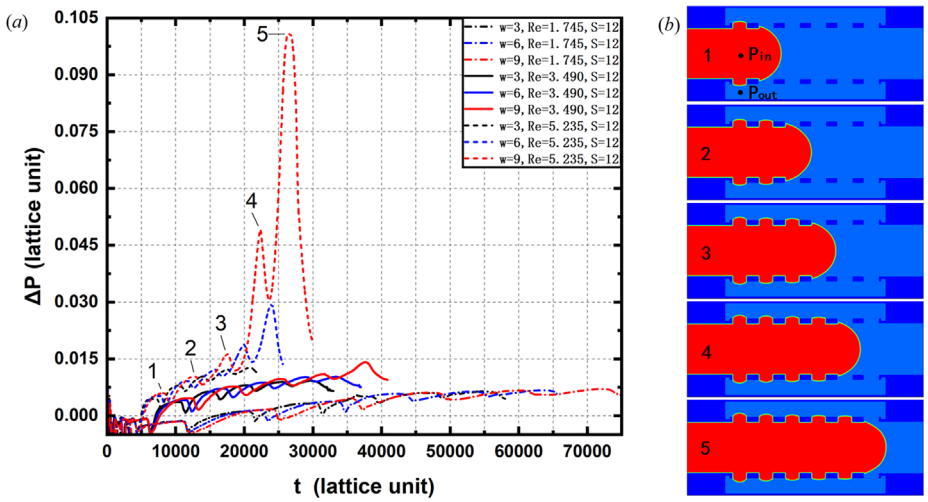

FIG. 18. (a) Pressure difference profiles at selected points for OPTI-DR-TPS. (b) Interface morphology at peak pressure differences under the conditions of $w = 9$, $Re = 5.235$, and $S = 12$.

microchannels were monitored through experiments. The composite structure was found to be beneficial to maintaining a stable gas–liquid interface. Using the LBM to simulate the flow of liquid in the microchannels, we found that the transverse posts block the path of liquid infiltration along the wall to the bottom of the groove and provide a pinning point for the liquid, thereby improving the stability of the gas–liquid interface. During the experiments and simulations, the gas–liquid interface exhibited two different collapse forms when flowing through the channels of the PR-TPS and DR-TPS at the same flow rate. Analysis of the collapse process enabled us to develop an improved design for the structure size and prove that this improvement significantly enhances the ability to maintain a stable interface. Finally, the influence of the structure dimensions on the stability of the gas–liquid interface was explored, providing guidance for the design of optimal structure dimensions for satisfying different flow requirements in practical applications.

ACKNOWLEDGMENTS

This research was supported by the National Natural Science Foundation of China (Grant No. 11872362) and the National Key R&D Program of China (Grant No. 2022YFE03130002).

AUTHOR DECLARATIONS

Conflict of Interest

The authors have no conflicts to disclose.

Author Contributions

Ming Zhu: Formal analysis (equal); Investigation (equal); Software (equal); Writing – original draft (equal). **Jian Huang:** Conceptualization (equal); Investigation (equal); Writing – original draft (equal). **Qiang Zhou:** Software (equal); Writing – review & editing (equal). **Zhaohui Yao:** Conceptualization (equal); Funding acquisition (equal); Methodology (equal); Supervision (equal); Writing – review & editing (equal).

DATA AVAILABILITY

The data that support the findings of this study are available from the corresponding authors upon reasonable request.

APPENDIX: CODE VALIDATION

To demonstrate the accuracy of the code, the ability to calculate the gas–liquid interface by Laplace's law is tested. A bubble is placed in the periodic cube region filled with liquid. As shown in Fig. 19(a), the blue area represents the bubble, the gray area represents the liquid, and the mesh size is $100 \times 100 \times 100$. At the initial moment, the density of component 1 (gas) inside and outside the bubble is 1.1422 and 0.020 66, respectively, while the density of component 2 (water) inside and outside the bubble is 0.020 66 and 1.1422, respectively. As the initial densities of the two components inside and outside the bubble cannot maintain the system in a steady state, the system automatically tends to a steady state due to the interaction between the two components. When the system reaches a stable state, the bubble radius and the pressure difference can be measured. Figure 19(b) shows the density field distribution at the central section after the system has reached the steady state. The black arrows represent velocity vectors, and we can clearly see the pseudo-velocity at the gas–liquid two-phase interface. The maximum pseudo-lattice velocity is 0.006. Generally, the pseudo-lattice velocity of the MCMP model is within the range of 0.05–0.1.[43] Therefore, the pseudo-lattice velocity in our case is reasonable. Figure 19(c) shows the pressure distribution along the y direction at $x = L/2$, $z = L/2$, where L is the side length of the cube. At the gas–liquid interface, significant changes in density cause sharp pressure changes, resulting in nonphysical fluctuations. Similar fluctuations have been observed in previous simulations[44] using the MCMP model. Such nonphysical fluctuations are ignored when calculating the pressure difference in this paper. Huang *et al.*[45] found that the density at the two-phase interface exhibits similar fluctuations when using Shan and Chen's model to simulate multicomponent systems. However, when using the free energy model to simulate

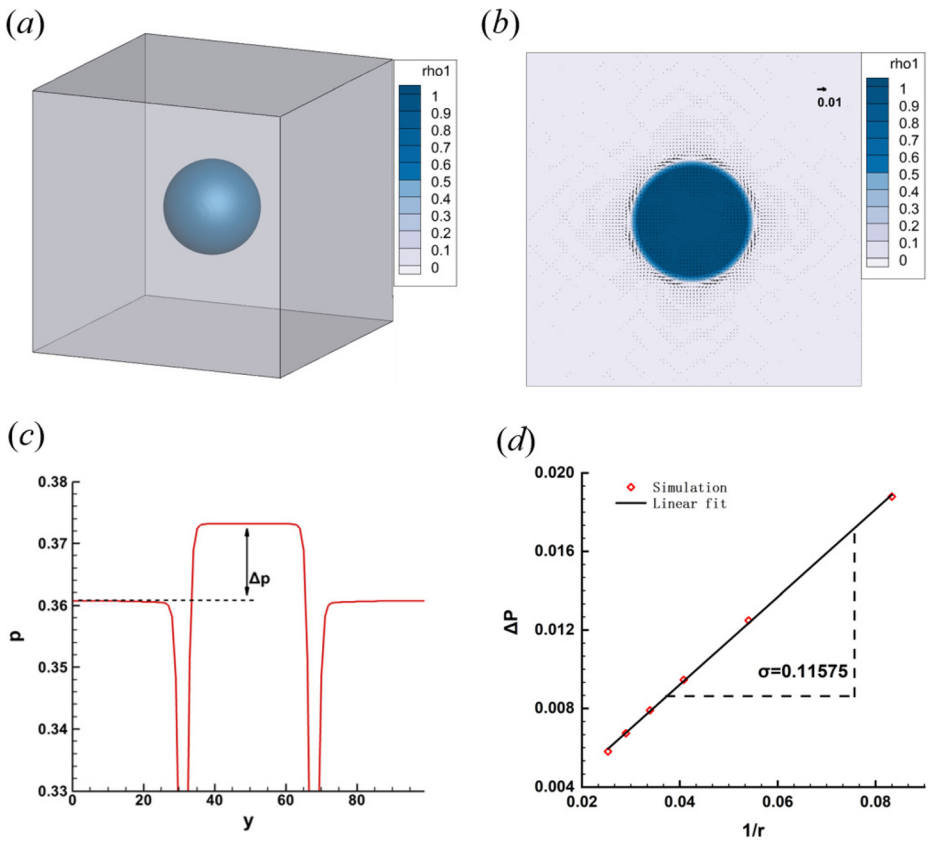

FIG. 19. (a) Initial distribution of a two-phase system. (b) Density distribution field and velocity vectors. (c) Pressure distribution along the center of the computational domain. (d) Dependence of pressure on radius and calibration of Laplace's law.

the same system, there are no density fluctuations at the interface. Huang *et al.* suggested that these nonphysical fluctuations were caused by the pseudovelocity at the interface. Figure 19(d) shows a clear linear relationship between the pressure difference and the bubble radius, which satisfies Laplace's law and verifies the accuracy of the code. The slope in the figure is 0.2315. Thus, we obtain $\sigma = 0.115\,75$, which can be obtained by the formula $\Delta P = \frac{2\sigma}{r}$.

To further verify the code's simulation effect on the evolution of gas–liquid interfaces in microstructures, we conduct corresponding simulations using the three types of structures considered in the experiments and compare them with the experimental results. Three different grid sizes are used, namely, $159 \times 80 \times 32$ (coarse), $318 \times 152 \times 32$ (medium), and $477 \times 224 \times 20$ (fine). As the channel height has little influence on the flow, the number of nodes in the height direction is the same in the coarse and medium grids and is reduced to 20 in the fine grid to reduce the computation time and save resources. The simulation results are shown in Fig. 20. The dark-blue area is the solid area, the light-blue area is air, and the red area is liquid. The simulated microchannel size and the actual microchannel size satisfy the geometric similarity law. At the initial moment, the channel is filled with air, and the liquid flows in from the left inlet at a constant *Re* number. The flow rate of the water injected into the channel is 50 μL/min in the experiment. The channel width is 200 μm, the channel height is 160 μm, and the physical parameters of water at room temperature are $\mu = 2.98 \times 10^{-3}$ Pa s and $\rho = 1000\,\mathrm{kg/m^3}$. Thus, we can calculate $Re = 1.745$.

The LBM results and the experimental results are compared in Fig. 20. Figures 20(a)–20(c) correspond to NR-TPS, PR-TPS, and DR-TPS, respectively. The first row is the experimental result. The following three rows represent the simulation results using the coarse, medium, and fine grids, respectively. The grid resolution increases from top to bottom, and each column represents the liquid surface morphology at the same dimensionless time $t^* = tu/L$, where u is the liquid velocity at the entrance, and L is the channel width at the entrance. Figure 20(a) represents the results of NR-TPS. When the de-ionized water is injected from the left side of the channel, the liquid infiltrates along the groove wall because the surface of the microchannel is hydrophilic. At $t^* = 0.9$, about two-thirds of the sidewall of the groove has been infiltrated by water. Subsequently, the liquid contacts the bottom of the groove and continues to infiltrate forward. During this process, the post provides a pinning point for the liquid, resulting in the interface forming a "w" shape, as shown at $t^* = 2.78$. When the liquid approaches the outlet of the channel, the channel suddenly narrows and the liquid flows in an asymmetric form, as shown at $t^* = 3.67$. Figures 20(b) and 20(c) show the results for PR-TPS and DR-TPS, respectively. The reentrant structure provides a pinning point for the liquid, preventing the liquid from continuing to infiltrate along the groove sidewall toward the groove bottom at the entrance. Subsequently,

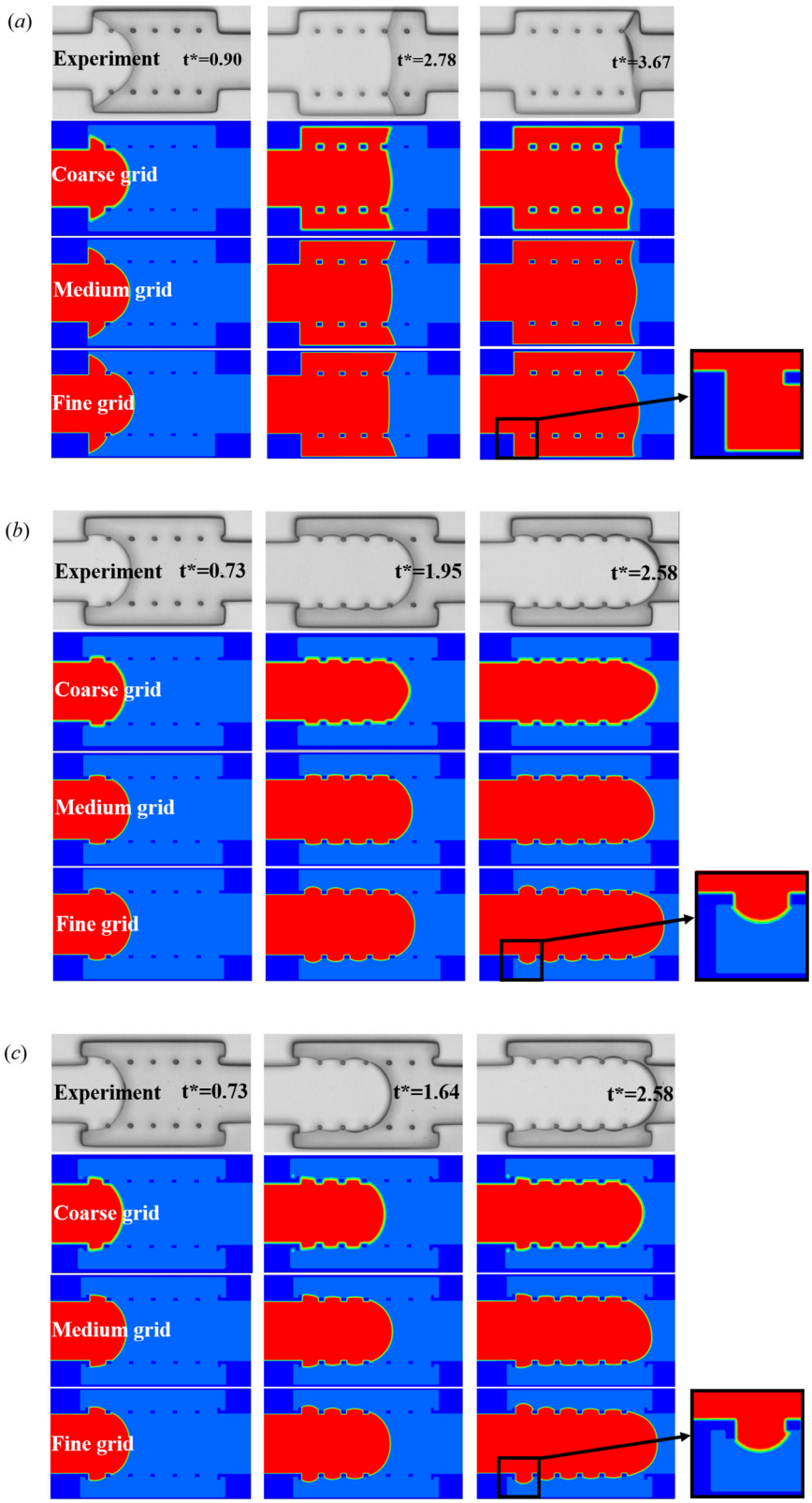

FIG. 20. Comparison between simulation results and experimental results: (a) NR-TPS; (b) PR-TPS; and (c) DR-TPS.

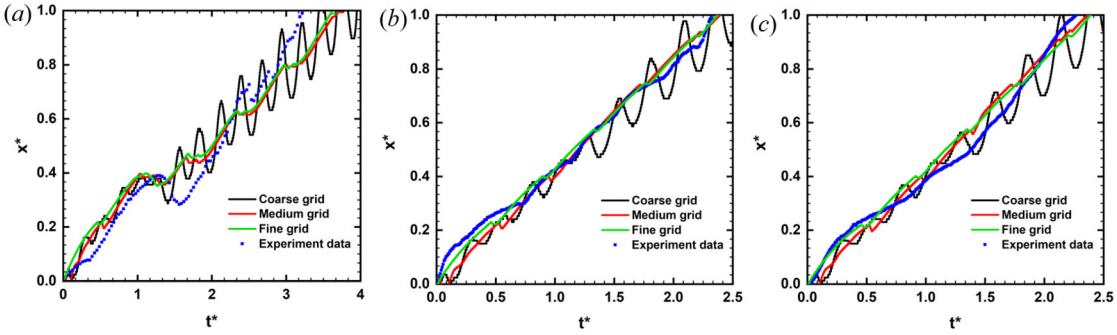

FIG. 21. Profiles of the gas–liquid interface coordinates at the central axis. x^* represents the dimensionless coordinates of the gas–liquid interface at the central axis. $x^* = \frac{x-x_1}{x_2-x_1}$, where x is the coordinate of the gas–liquid interface at the central axis, x_1 is the coordinate of the microstructure inlet, and x_2 is the coordinate of the microstructure outlet; t^* is the dimensionless time.

the liquid flows by all posts in sequence and forms a stable pinning on the reentrant structure at the outlet. Comparing the simulation results with the experimental results, the LBM effectively describes the interface morphology and the interface evolution process in microchannels.

To analyze the impact of different grid sizes quantitatively, the coordinates of the gas–liquid interface at the central axis are traced. As shown in Fig. 21, x^* is the dimensionless coordinate computed as $x^* = \frac{x-x_1}{x_2-x_1}$, where x is the coordinate of the gas–liquid interface at the central axis, x_1 is the coordinate of the microstructure inlet, and x_2 is the coordinate of the microstructure outlet; t is the dimensionless time. Although the coarse grid can describe the interface morphology, the interface exhibits nonphysical oscillations, which are inconsistent with the experiment. Both the medium and fine grids accurately describe the evolution of the gas–liquid interface and are in good agreement with the experimental results. In the PR-TPS, the errors from using the medium grid and the fine grid compared with the experimental results are 8.2% and 4.29%, respectively. In the DR-TPS, the corresponding errors are 9.3% and 7.6%, respectively. Therefore, considering computational efficiency, we adopt the medium grid in our research.

REFERENCES

[1]J. Ou, B. Perot, and J. P. Rothstein, "Laminar drag reduction in microchannels using ultrahydrophobic surfaces," Phys. Fluids **16**, 4635 (2004).
[2]J. Ou and J. P. Rothstein, "Direct velocity measurements of the flow past drag-reducing ultrahydrophobic surfaces," Phys. Fluids **17**, 103606 (2005).
[3]C. Lee, C.-H. Choi, and C.-J. Kim, "Superhydrophobic drag reduction in laminar flows: A critical review," Exp. Fluids **57**, 176 (2016).
[4]A. V. Belyaev and O. I. Vinogradova, "Effective slip in pressure-driven flow past super-hydrophobic stripes," J. Fluid Mech. **652**, 489 (2010).
[5]C. J. Teo and B. C. Khoo, "Flow past superhydrophobic surfaces containing longitudinal grooves: Effects of interface curvature," Microfluid. Nanofluid. **9**, 499 (2010).
[6]A. M. J. Davis and E. Lauga, "Hydrodynamic friction of fakir-like superhydrophobic surfaces," J. Fluid Mech. **661**, 402 (2010).
[7]S. Arunachalam, Z. Ahmad, R. Das, and H. Mishra, "Counterintuitive wetting transitions in doubly reentrant cavities as a function of surface make-up, hydrostatic pressure, and cavity aspect ratio," Adv. Mater. Interfaces **7**, 2001268 (2020).
[8]J. Hyvaluoma and J. Harting, "Slip flow over structured surfaces with entrapped microbubbles," Phys. Rev. Lett. **100**, 246001 (2008).
[9]D. Dilip, M. S. Bobji, and R. N. Govardhan, "Effect of absolute pressure on flow through a textured hydrophobic microchannel," Microfluid. Nanofluid. **19**, 1409 (2015).
[10]Y. Xue, P. Lv, Y. Liu, Y. Shi, H. Lin, and H. Duan, "Morphology of gas cavities on patterned hydrophobic surfaces under reduced pressure," Phys. Fluids **27**, 092003 (2015).
[11]T. J. Kim and C. Hidrovo, "Pressure and partial wetting effects on superhydrophobic friction reduction in microchannel flow," Phys. Fluids **24**, 112003 (2012).
[12]P. Lv, Y. Xue, Y. Shi, H. Lin, and H. Duan, "Metastable states and wetting transition of submerged superhydrophobic structures," Phys. Rev. Lett. **112**, 196101 (2014).
[13]Y. Xiang, Y. Xue, P. Lv, D. Li, and H. Duan, "Influence of fluid flow on the stability and wetting transition of submerged superhydrophobic surfaces," Soft Matter **12**, 4241 (2016).
[14]S. Huang, P. Lv, and H. Duan, "Morphology evolution of liquid–gas interface on submerged solid structured surfaces," Extrem. Mech. Lett. **27**, 34 (2019).
[15]P. Forsberg, F. Nikolajeff, and M. Karlsson, "Cassie–Wenzel and Wenzel–Cassie transitions on immersed superhydrophobic surfaces under hydrostatic pressure," Soft Matter **7**, 104 (2011).
[16]Y. Xiang, S. Huang, P. Lv, Y. Xue, Q. Su, and H. Duan, "Ultimate stable underwater superhydrophobic state," Phys. Rev. Lett. **119**, 134501 (2017).
[17]Y. Xue, S. Chu, P. Lv, and H. Duan, "Importance of hierarchical structures in wetting stability on submersed superhydrophobic surfaces," Langmuir **28**, 9440 (2012).
[18]A. Tuteja, W. Choi, M. Ma, J. M. Mabry, S. A. Mazzella, G. C. Rutledge, G. H. McKinley, and R. E. Cohen, "Designing superoleophobic surfaces," Science **318**, 1618 (2007).
[19]T. L. Liu and C. J. Kim, "Repellent surfaces. Turning a surface superrepellent even to completely wetting liquids," Science **346**, 1096 (2014).
[20]H. Shams, K. Basit, M. A. Khan, S. Saleem, and A. Mansoor, "Realizing surface amphiphobicity using 3D printing techniques: A critical move towards manufacturing low-cost reentrant geometries," Addit. Manuf. **38**, 101777 (2021).
[21]X. Liu, H. Gu, M. Wang, X. Du, B. Gao, A. Elbaz, L. Sun, J. Liao, P. Xiao, and Z. Gu, "3D printing of bioinspired liquid superrepellent structures," Adv. Mater. **30**, e1800103 (2018).
[22]S. Hu, X. Cao, T. Reddyhoff, D. Puhan, S. C. Vladescu, J. Wang, X. Shi, Z. Peng, A. J. deMello, and D. Dini, "Liquid repellency enhancement through flexible microstructures," Sci. Adv. **6**, eaba9721 (2020).
[23]R. Das, Z. Ahmad, J. Nauruzbayeva, and H. Mishra, "Biomimetic coating-free superomniphobicity," Sci. Rep. **10**, 7934 (2020).
[24]J. Zhang, Z. Yao, and P. Hao, "Formation and evolution of air–water interfaces between hydrophilic structures in a microchannel," Microfluid. Nanofluid. **21**, 135 (2017).

[25]J. R. Panter, Y. Gizaw, and H. Kusumaatmaja, "Multifaceted design optimization for superomniphobic surfaces," Sci. Adv. **5**, eaav7328 (2019).
[26]C. Lee and C. J. Kim, "Underwater restoration and retention of gases on superhydrophobic surfaces for drag reduction," Phys. Rev. Lett. **106**, 014502 (2011).
[27]Y. Xiang, S. Huang, T. Y. Huang, A. Dong, D. Cao, H. Li, Y. Xue, P. Lv, and H. Duan, "Superrepellency of underwater hierarchical structures on Salvinia leaf," Proc. Natl. Acad. Sci. U. S. A. **117**, 2282 (2020).
[28]D. Raabe, "Overview of the lattice Boltzmann method for nano- and microscale fluid dynamics in materials science and engineering," Modell. Simul. Mater. Sci. Eng. **12**, R13 (2004).
[29]Y. He, Q. Li, Y. Wang, and G. Tang, "Lattice Boltzmann method and its applications in engineering thermophysics," Chin. Sci. Bull. **54**, 4117 (2009).
[30]H. Huang, M. C. Sukop, and X. Lu, *Multiphase Lattice Boltzmann Methods: Theory and Application* (Wiley, New York, 2015).
[31]J. P. Boon and S. Succi, *The Lattice Boltzmann Equation for Fluid Dynamics and Beyond* (Clarendon Press, Oxford, 2001).
[32]T. Krüger, H. Kusumaatmaja, A. Kuzmin, O. Shardt, and E. M. Viggen, *The Lattice Boltzmann Method - Principles and Practice* (Springer, Berlin, 2016).
[33]U. Frisch, B. Hasslacher, and Y. Pomeau, "Lattice-gas automata for the Navier–Stokes equation," Phys. Rev. Lett. **56**, 1505 (1986).
[34]Z. Guo and C. Zhen, *Theory and Applications of Lattice Boltzmann Method* (Science Press, Beijing, 2009).
[35]A. K. Gunstensen, D. H. Rothman, S. Zaleski, and G. Zanetti, "Lattice Boltzmann model of immiscible fluids," Phys. Rev. A **43**, 4320 (1991).
[36]X. Shan and H. Chen, "Simulation of nonideal gases and liquid–gas phase transitions by the lattice Boltzmann equation," Phys. Rev. E **49**, 2941 (1994).
[37]M. R. Swift, W. R. Osborn, and J. M. Yeomans, "Lattice Boltzmann simulation of nonideal fluids," Phys. Rev. Lett. **75**, 830 (1995).
[38]X. He, X. Shan, and G. Doolen, "Discrete Boltzmann equation model for nonideal gases," Phys. Rev. E. **57**, R13 (1998).
[39]X. W. Shan and G. Doolen, "Multicomponent lattice-Boltzmann model with interparticle interaction," J. Stat. Phys. **81**, 379 (1995).
[40]Q. Zhang, D. Sun, Y. Zhang, and M. Zhu, "Lattice Boltzmann modeling of droplet condensation on superhydrophobic nanoarrays," Langmuir **30**, 12559 (2014).
[41]D. A. Wolf-Gladrow, *Lattice-Gas Cellular Automata and Lattice Boltzmann Models - An Introduction* (Springer, Berlin, 2000).
[42]M. Li, C. Huber, Y. Mu, and W. Tao, "Lattice Boltzmann simulation of condensation in the presence of noncondensable gas," Int. J. Heat Mass Transfer **109**, 1004 (2017).
[43]J. Bao and L. Schaefer, "Lattice Boltzmann equation model for multicomponent multi-phase flow with high density ratios," Appl. Math. Model. **37**, 1860 (2013).
[44]L. Chen, Q. Kang, Q. Tang, B. A. Robinson, Y.-L. He, and W.-Q. Tao, "Pore-scale simulation of multicomponent multiphase reactive transport with dissolution and precipitation," Int. J. Heat Mass Transfer **85**, 935 (2015).
[45]H. Huang, L. Wang, and X-y Lu, "Evaluation of three lattice Boltzmann models for multiphase flows in porous media," Comput. Math. Appl. **61**, 3606 (2011).